

The rise and sink dependence on the shape of a horizontally wiggling intruder

Bitang Kwrung Tripura¹ Sonu Kumar², Vamsi Krishna Reddy Anyam³ and K. Anki Reddy^{4†}

¹Department of Chemical Engineering, Indian Institute of Technology, Guwahati, Assam, 781039, India

²Department of Chemical and Biomolecular Engineering, University of Notre Dame, Notre Dame, Indiana 46556, USA

³Department of Chemical Engineering, Indian Institute of Science, Bangalore 560 012, India

⁴Department of Chemical Engineering, Indian Institute of Technology, Tirupati, AndhraPradesh, 517619, India

(Received xx; revised xx; accepted xx)

We investigate the effect of shape and orientation for a horizontally oscillating intruder on its vertical dynamics in a granular medium via Discrete Element Method (DEM) simulations. Five distinct intruder shapes were considered in this study: a disk (OS1), a square (OS2), two rectangles with aspect ratios > 1 (OS3) and < 1 (OS4) respectively, and an equilateral triangle (OS5). The vertical velocity of the oscillating object was observed to be a function of amplitude and frequency (f)/time period (T) of oscillation and the shape of the object. The dynamics of the motion are modelled with the help of a cavity-based model, which can empirically produce the regimes observed by incorporating the free-fall of the particles filling the cavity. The cavity-based model assumes that there is a point on the surface of each oscillating object unique to its shape that any grain crossing it will irreversibly reach the bottom of the cavity. This leads to the creation of a bed of particles at the bottom of the cavity, which increases the intruder's elevation as it oscillates, leading to its vertical rise in the granular medium. In addition, we observed a minimum amplitude (A_{\min}) below which the vertical position of the intruder remains unaltered for various T . Among all the shapes, disk (OS1) displays the highest rising rate while triangle (OS5) shows the highest sinking rate. The cavity model can integrate the effect of shape and guess the efficiency of one shape over another in the rising dynamics. We have also presented the time-averaged pressure P , velocity V , and area fraction Φ fields around the intruder shapes.

1. Introduction

Animals native to deserts have an extreme shortage of food and water, making any wastage of energy detrimental to them. As such, their bodies have undergone evolutionary changes to have the optimal shape required to walk on the surface or even exhibit subsurface motion with minimum loss of energy. For example, sand lizards (Maladen *et al.* 2009; Goldman & Hu 2010; Sharpe *et al.* 2013) and sidewinder snakes (Marvi *et al.* 2014; Zhu *et al.* 2021) employ a wiggling motion to move in the sand. A comprehensive understanding of this kind of motion has various applications in sub-terrain robotics (Raibert *et al.* 2008; Zhang *et al.* 2013), in rescue operations through sand or snow (Urquhart 2010), and in mining related operations.

† Email address for correspondence: anki.reddy@iittp.ac.in

The subsurface motion of animals has garnered interest in the fields of earth-sciences (Clark *et al.* 2012, 2014), biology (Maladen *et al.* 2009; Mazouchova *et al.* 2010; Goldman 2014; Sharpe *et al.* 2015), and engineering (Hu *et al.* 2009; Meirion-Griffith & Spenko 2010; Li *et al.* 2013) owing to its interesting dynamics. To understand the mechanism behind their movement through the granular medium, researchers (Maladen *et al.* 2009; Sharpe *et al.* 2013) conducted laboratory experiments on the creatures. Maladen *et al.* (2009) studied how a sand lizard moves within the granular media with the help of high-speed x-ray imaging. Surprisingly, they noticed that the lizard does not use its limbs for propulsion, but it generates thrust by propagating a wavy motion of its body once it is under the surface. Sharpe *et al.* (2013) investigated the neuromechanical movement of sandfish lizard during its walking above the surface or sand swimming under the surface of a granular medium with the help of visible light imaging using electromyogram (EMG). The authors reported that the frictional forces play a prominent role in resisting the intrusion of the creatures. Moreover, they observed that the resistance to the undulatory motion of the creatures increases with the depth. Despite the resistance, the sand-dwelling creatures have adopted certain mechanisms to move within the bed of granular particles. Maladen *et al.* (2011*a,b*) have tried to comprehend this phenomenon by developing sand swimming robots. The ratio of forwarding speed to the wave speed of a robot was noticed (Maladen *et al.* 2011*a*) to increase with an increase in the inter-particle friction but decreases with an increase in the particle-robot friction. In addition, Maladen *et al.* (2011*b*) investigated various head shapes of the robot and their influence on the drag-induced lift. The authors noticed that for certain wedge shapes of the robot, it reaches the free surface whereas, for other ones, it sinks to the bottom, indicating the importance of the robot's shape on its rise/sink dynamics. Apart from these studies, to gain a better insight into the creatures' movement within granular media, they have been modelled as self-energized objects.

Few recent studies focused on understanding the dynamics of a self-energized object in granular media either translating ((Ding *et al.* 2011; Guillard *et al.* 2014; Kumar *et al.* 2017; Tripura *et al.* 2021)) or oscillating horizontally in both two (Huang *et al.* (2016)) and three-dimensional systems (Ping *et al.* (2020), Liu *et al.* (2021)). Huang *et al.* (2016) explained the mechanism behind the rise and sink of a horizontally oscillating circular intruder in a two-dimensional system with the help of a mathematical model. They stated that the amplitude and frequency at which the intruder object oscillates mainly contribute to its rise or sink. They have also reported a minimum oscillation amplitude (A_{\min}) below which the intruder does not sink irrespective of its frequency. Ping *et al.* (2020) noticed that the intruder rises at low amplitude rates and sinks at high amplitude rates. They also found that an intruder might either rise or sink or remain at the same initial vertical position depending on its oscillating frequency and amplitude in a three-dimensional system. Further, the authors explained the driving mechanisms such as fluidization or cavity formation behind the intruder's vertical dynamics.

The previous studies were concerned mostly with the sole effect of the intruder's horizontal wiggling motion on its vertical dynamics. However, a coupled effect of wiggling motion along with other properties of the intruder can enhance the rise/sink dynamics. To this extent, Liu *et al.* (2021) studied the combined effect of rotation and oscillation of a spherical intruder on its rise/sink dependence within a three-dimensional granular media. The effect of intruder's shape, coupled with its wiggling motion has not been studied to the best of our knowledge. In this regard, we numerically investigated how the shape of the intruder affects its vertical motion induced by horizontal wiggling. We studied how the oscillation parameters affect their vertical dynamics for each of these shapes. Further, we probed the influence of the properties of the granular medium, such

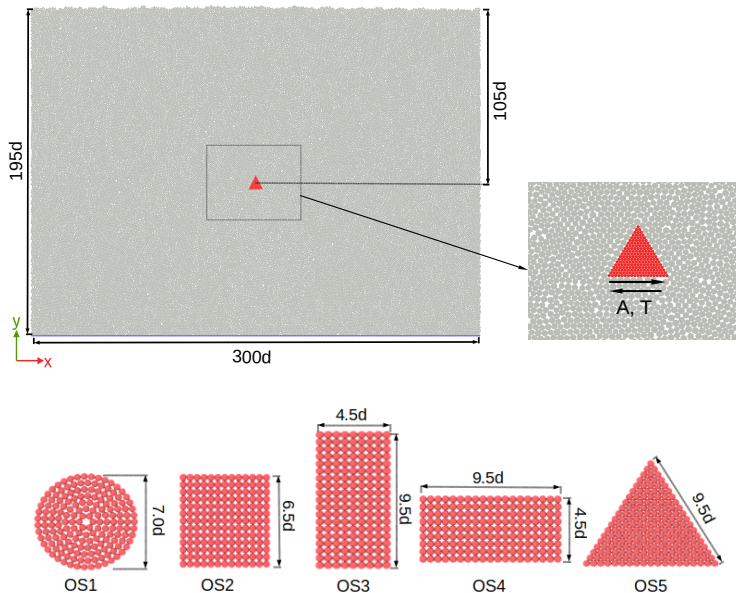


Figure 1: Initial configuration with one of the intruders (triangle) placed in the center (taken as origin) of the system and at a depth $h = 105d$ from the free surface. The base is made of particles of size $1d$ (blue particles) at $y = 0$ while the top surface is free to move and periodic boundary conditions are applied in x direction. The intruder shapes that are considered in our study are disk OS1, square OS2, rectangle with its longer dimension along the y -axis OS3, rectangle with its longer dimension along the x -axis OS4, and equilateral triangle OS5. The intruder is oscillated horizontally with a velocity $V_x = A \sin(2\pi t/T)$ where A , T represents the amplitude and the time period of oscillation and t is the time elapsed.

as the coefficient of friction on the intruder's vertical motion. Finally, we proposed a mathematical model that predicts the intruder's rise/sink dynamics depending on its shape and the oscillation parameters.

2. Simulation methodology

To study the dynamics of a horizontally oscillating intruder within a two-dimensional granular medium, we used the discrete element method (Cundall & Strack (1979)). Figure 1 shows the initial configuration of our system having dimensions of $300d \times 195d$ along the x and the y -axis respectively, where d is the mean particle diameter. The intruder is placed at a depth of $105d$ from the free surface and at the centre of the simulation system. A set of particles are introduced uniformly at the top of the system which gets settled at the bottom due to gravity, while keeping the intruder stationary. Then, another set of particles are introduced and so on until the height of the granular bed reaches $195d$. The total number of particles comprising the system at the end is $N_t = 63000$. The diameter of the particles ranges from $0.9d$ to $1.1d$ to avoid crystallization and while pouring and

settling, we ensured that there are no overlaps among the particles. We further continued the simulation until the total kinetic energy of all the particles in the system have reached almost zero. At time $t = 0$, the intruder is oscillated horizontally with a velocity $V_x = A \sin(2\pi t/T)$ where A , T represents the amplitude, and the time period of oscillation and t is the time elapsed. In our work, we have considered five different shaped intruders, which are pictorially represented in figure 1. Each of the individual intruder shapes is created by gluing a set of spherical particles having a diameter of $0.5d$ in such a way that their entire mass is the same for all the shapes.

In the discrete element method (DEM), the positions and the velocities of particles are updated at regular intervals of time by integrating the equations of motion. The forces considered are the contact force and the body force. The normal F_{ij}^n and the tangential F_{ij}^t components of contact force between two particles i and j at a given time t , is calculated using the contact force model (Brilliantov *et al.* (1996); Silbert *et al.* (2001)), as shown in equations 2.1 and 2.2. According to the model, two particles i and j are said to be in contact if the overlap is $\delta \geq 0$, where $\delta = R_i + R_j - r_{ij}$. Here, R_i , R_j are the radii of the two contacting particles, and r_{ij} is the instantaneous distance between the centres of the two particles.

$$F_{ij}^n = \sqrt{(R_{\text{eff}}\delta_{ij})(K_n\delta_{ij}\hat{n}_{ij} - m_{\text{eff}}\gamma_n v_{ij}^n)} \quad (2.1)$$

$$F_{ij}^t = -\min(\mu F_n, \sqrt{(R_{\text{eff}}\delta_{ij})(K_t\Delta s_t + m_{\text{eff}}\gamma_t v_{ij}^t)}) \quad (2.2)$$

Here, $K_n = 2 \times 10^6 \rho dg$ and $K_t = 2.46 \times 10^6 \rho dg$ are the nonlinear spring constants, where ‘n’ and ‘t’ in the subscripts or superscripts correspond to normal and tangential components of respective parameters. Here, v_{ij} is relative velocity, and \hat{n}_{ij} is a unit vector in the direction of the line joining the centres of particles i and j . The damping coefficients γ_n and γ_t are set to $2500\sqrt{g/d^3}$ and Δs_t is the tangential displacement vector between the two particles in contact. The effective mass m_{eff} and the effective radius R_{eff} for a given pair of contacts are expressed as $\frac{m_i m_j}{m_i + m_j}$ and $\frac{R_i R_j}{R_i + R_j}$ respectively. The maximum value F_{ij}^t can reach is μF_{ij}^n because, at this threshold, the particles slip due to the dynamic friction. The time-step is $\Delta t = 1 \times 10^{-4} \sqrt{d/g}$ for all cases. The coefficient of friction μ is 0.1 for all the simulations unless specified. Each of the simulations was performed for a run time of $10^7 \Delta t$ to maintain parity among all the calculated results. The simulations are performed using dimensionless units, by considering acceleration due to gravity g , mean particle diameter d , and density ρ as the basic units. The values of d , ρ , and g are set to 1.0 without loss of generality. All the simulations are carried out using the Large-scale Atomic/Molecular Massively Parallel Simulator (LAMMPS) (<https://www.lammps.org>, Plimpton (1995)), and for the visualization, OVITO package (Stukowski (2010)) has been utilized.

3. Results and Discussion

In this section, we presented the numerical results obtained for five different intruder shapes subjected to different oscillation parameters. We horizontally oscillated each intruder at different constant amplitudes $A/d = 0.5, 1, 3, 5$ and at various constant time periods T ranging from 0.25 to 8. This section is organized as follows: Subsection 3.1 demonstrates the vertical displacement of each intruder as a function of time at various time periods T and for an amplitude $A/d = 3$. The average rate of vertical displacement

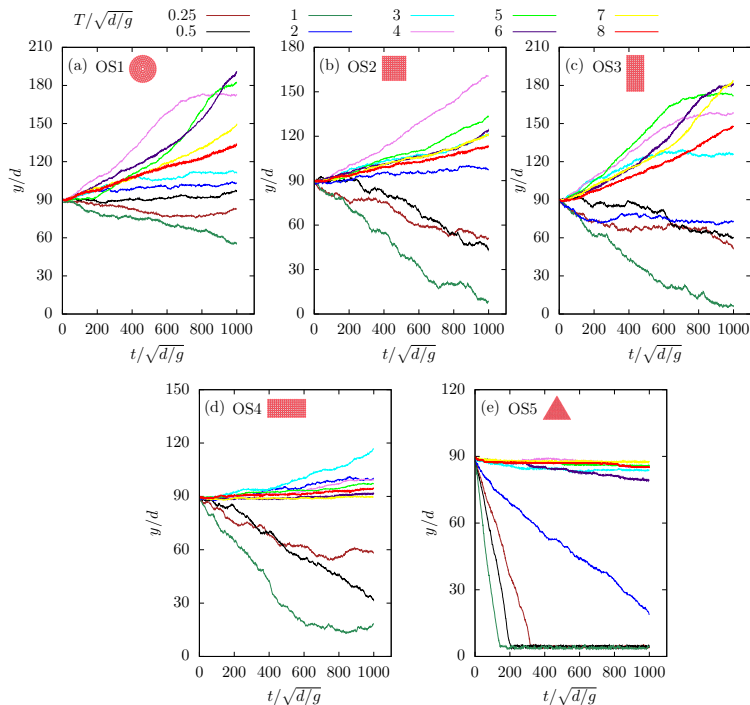


Figure 2: The vertical displacement of the intruder (a) disc, (b) square, (c) narrow-rectangle, (d) wide-rectangle, and (e) triangle shapes as a function of simulation time(t) for an oscillation amplitude $A/d=3$ and at different time period ($T/\sqrt{d/g}$).

V_y dependence on the intruder's shape at different A/d , T and μ is discussed in subsection 3.2. In subsection 3.3, we showed the average rate of vertical displacement of the intruder as a function of the oscillating phase-angle φ . In subsection 3.4, we elucidated the mean flow fields around the intruder. Lastly, in subsection 3.5, we have compared our results with the proposed mathematical model and explained the physical phenomenon leading to the rise and sink of the intruder for different parameters considered in the study.

3.1. Vertical displacement of oscillating intruder

In this subsection, we showed the vertical displacement of the intruders as a function of the simulation time t for an amplitude of $A/d = 3$ at different time-periods $T/\sqrt{d/g}$. Figure 2 a shows the vertical displacement of a disk-shaped intruder OS1 oscillated at different T . At time periods of oscillation $T \geq 2$, a wake is formed either to the left side of the intruder or to the right side, depending on its direction of motion. In this sense, when the intruder moves from left to right, the wake is developed to the left side of the intruder. When the intruder changes its direction of oscillation and starts to move from right to left, it interacts with the wake that is on its left side. When the intruder reaches the middle point of oscillation, the wake to its left vanishes, and simultaneously another wake evolves to the intruder's right side. When the intruder is traversing the granular medium, the particles above the wake region tries to fill the wake due to the action of gravity. In the process, a bed of particles is created on the edges of the wake region. When the intruder changes its direction of motion, it must climb the bed of particles

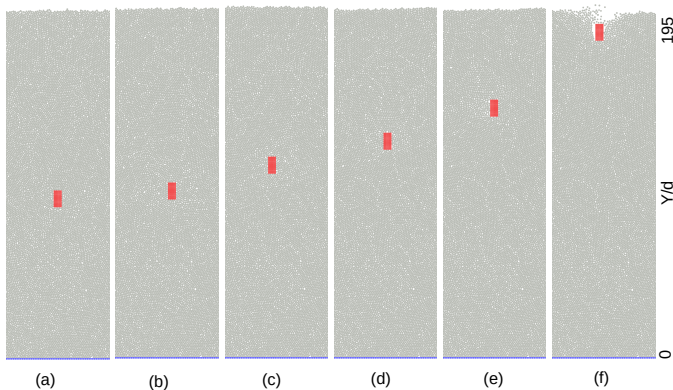


Figure 3: A pictorial representation depicting the position of the narrow-rectangle OS3 for $A/d=3$ and $T/\sqrt{d/g}=7$ at different simulation time $t/\sqrt{d/g}$: (a) 0 (b) 100 (c) 300 (d) 500 (e) 700 and (f) 1000.

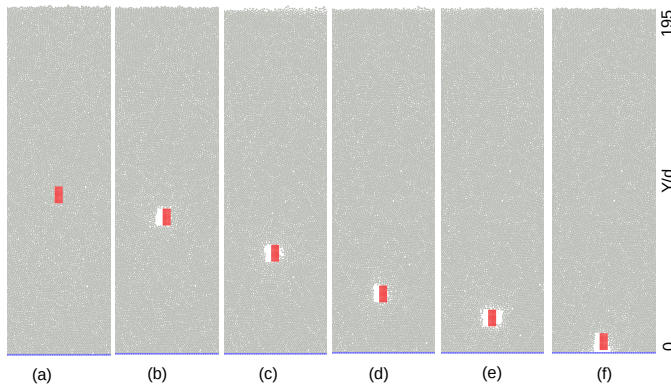


Figure 4: A pictorial representation depicting the position of the narrow-rectangle OS3 for $A/d=3$ and $T/\sqrt{d/g}=1$ at different simulation time $t/\sqrt{d/g}$: (a) 0 (b) 100 (c) 300 (d) 500 (e) 700 and (f) 1000.

to move ahead, and thus a vertical displacement of the intruder takes place. This is the reason behind the rise of the disk-shaped intruder at longer time periods. Interestingly, the intruder neither sinks nor rises at certain intermediate time-periods $T = 2$. At time periods T ranging from 0.25 to 1, the wake is formed not only beside the intruder but also above and below it. This is due to its high oscillation frequency and, consequently, a greater momentum transfer to the surrounding particles. The presence of the wake below the intruder propels it to sink due to the gravity acting on it. Thus, the disk-shaped intruder sinks at shorter time periods or larger frequencies of oscillation. Similar behavior has been observed in both 2D (Huang *et al.* 2016) and 3D (Ping *et al.* 2020) granular systems, where the disk (2D) and the spherical (3D) shaped intruders rise at lower frequencies and sink at higher frequencies of oscillation.

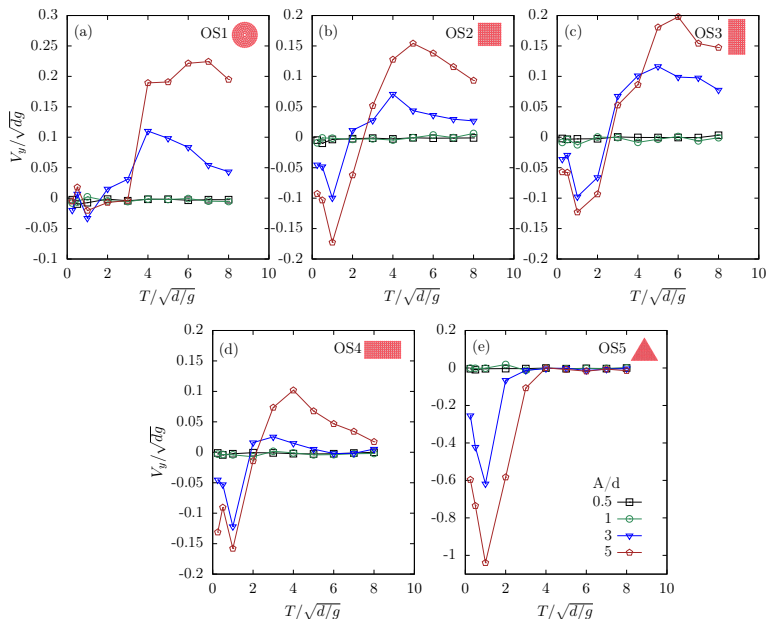


Figure 5: The rise rate (V_y) of the horizontally oscillating intruder as a function of its time-period (T) for different amplitude A . Here, each plot corresponds to a different intruder shape: (a) disk, (b) square, (c) narrow-rectangle, (d) wide-rectangle, and (e) triangle.

The square-shaped intruder shows similar behavior (figure 2 b) to that of the disk one (in supplementary information we have provided the links for the videos showing the rise and sink of the square shaped intruder when oscillated at time period of 5 and 1 within the granular medium). However, the square-shaped intruder is noticed to move to lower vertical distances than the disk one for longer time periods. This is due to the larger stress experienced by the square one (OS2) as compared to that of the disk one (OS1) from the particles above. The reason for it is due to the presence of a flat surface at the top of the square intruder and a curved one for the disk one. Figure 2 c shows the vertical displacement of a rectangle with a small base (OS3) whose behavior is like that of the disk and the square shapes. Though rectangle and square-shaped intruders have flat top surfaces, the former moves to a higher vertical distance than the latter one. The reason for this behavior is that the rectangle intruder (OS3) has a smaller top surface than the square one and hence a smaller stress from the particles above it. A pictorial representation of the rectangle intruder (OS3) is shown to depict this rise and sink phenomena at different simulation times $t/\sqrt{d/g}$ when oscillated at a higher time period ($T/\sqrt{d/g} = 7$) (figure 3) and at a lower one ($T/\sqrt{d/g} = 1$) (figure 4) for a given amplitude $A/d = 3$. Further, the rectangle with a larger base/top surface (OS4) moves upwards at a slower rate than (figure 2 d) that of the square one and the rectangle one with a smaller base (OS3). This is due to a larger top surface and consequently a higher stress from the particles above it. Interestingly, the sinking behavior is observed to be independent of the base length of the quadrilaterals (OS2, OS3 and OS4) considered in our study. The triangular intruder behaved differently as compared to all the other

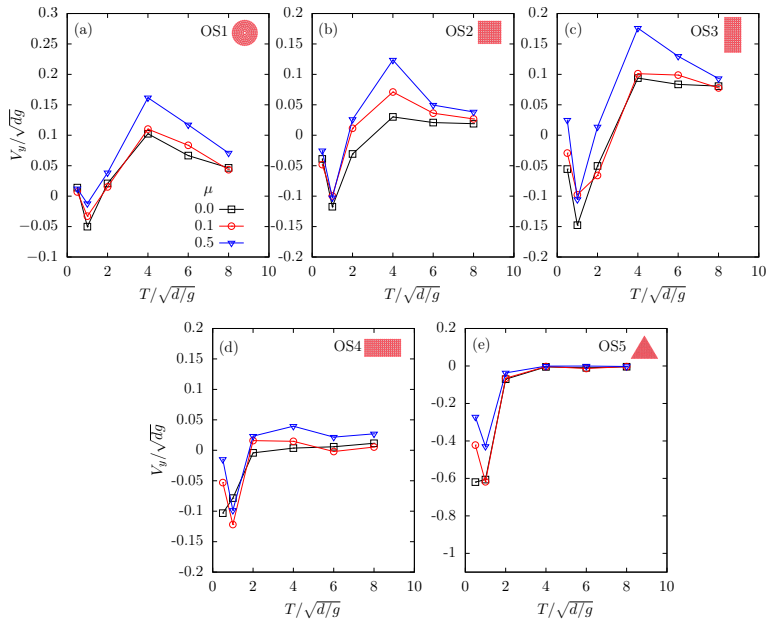


Figure 6: The rise rate (V_y) of the horizontally oscillating intruder as a function of its time-period (T) for different friction coefficient μ and amplitude $A/d = 3$. Here, each plot corresponds to a different intruder shape: (a) disk, (b) square, (c) narrow-rectangle, (d) wide-rectangle, and (e) triangle.

shapes. In this sense, the triangular intruder is noticed to sink always irrespective of the time periods (figure 2 e). In this case, a bed of particles is not created near the edges of the wake owing to the intruder's inclined sides and sharp edges. An intriguing observation is that the maximum vertical distance traversed by the intruder varies non-monotonically with the time period. Apart from the maximum vertical distance travelled by an intruder, how quickly an intruder can rise, or sink is equally important. This aspect of the intruder is discussed in the next subsection.

3.2. Rate of rise of intruder with time-period

In this subsection, we explain how the vertical displacement rate of an intruder varies with its shape and oscillation parameters. The rate of change of vertical displacement is defined as $V_y = (y_f - y_i)/(t_f - t_i)$. Here, y_i and y_f are the initial and final vertical positions of the intruder at times t_i and t_f . Note that t_i is considered at $1/10^{\text{th}}$ of the total simulation time ($1000\sqrt{d/g}$). For some cases, we noticed the intruder reaches its final vertical position before the end of the simulation ($1000\sqrt{d/g}$). An example of such behaviour can be seen in figure 2 a for a circular intruder at time period $T = 4$ for which $t_f = 650$. For these type of cases, we have taken t_f as the time at which the intruder is about to reach its final vertical position. Henceforth, the positive value of V_y implies the intruder is rising and the negative value of V_y corresponds to sinking. Figure 5 shows the intruder's rate of rise/sink as a function of time-period (T) and for amplitudes, $A/d = 0.5, 1, 3,$ and 5 . The rate of rise/sink is negligible at all time periods for the amplitudes (A) of 0.5 and 1 for all the intruder shapes. Similar behavior has been reported for a

oscillating disk in a previous work by Huang *et al.* (2016), where the authors reported that to facilitate the vertical motion of the intruder, a minimum amplitude of oscillation is necessary.

Figure 5 a shows a slightly negative V_y for $A/d = 3$ and at $T \leq 1$ for a disk-shaped intruder. This result is consistent with the negative vertical displacement observed in figure 2 a for $T \leq 1$. At $T \geq 2$, we observed a positive V_y for the range of time periods considered in our study. Surprisingly, as the time-period increases, the rise rate first increases, reaches a maxima and then decreases. When the intruder changes its direction of motion, it is impelled to climb over a bed of particles leading to its rise at large time periods. Suppose, if the intruder is moving from left to right, then the above-mentioned bed of particles corresponds to the ones that are trying to fill the wake which is formed just to the right of the intruder. These particles could be the ones that fall from above the intruder or the ones that are adjacent to the wake. As the time period increases, more particles get piled up, and consequently, the intruder has to climb over a larger set of particles. This leads to an increase in its vertical position and its rise rate. As time period increases, we noticed a maxima and then a decrease in the rise rate. The reason for this is at larger time periods, greater number of particles gets piled up which dampens the upward motion of the intruder. In summary, the group of particles falling behind the intruder, or in other words, the size of the bed of particles behind it, is responsible for the non-monotonic behavior of the intruder's rise rate. Even at amplitude $A/d = 5$, the non-monotonic behavior in the rise rate is noticed. Moreover, the rise rate increases with an increase in the amplitude.

The rate of rise/sink of a square intruder (OS2) as a function of the time period is shown in figure 5 b. At time periods $T \leq 2$, amplitude $A/d = 3$, the square intruder has a negative rate of vertical displacement or sink rate. Interestingly, as the T increases, the sink rate gradually increases reaching a maxima and then decreases. At $T < 2$, a wake is formed not only on either sides of the intruder but also above and below it as a result of a high frequency of oscillation. The action of gravity on the intruder coupled with a low area fraction of particles below it results in its sinking. As the time period increases, the size of the wake above the intruder decreases, and consequently, the number of particles interacting, or in other words, the stress exerted on the top surface of the intruder increases. This results in an increase in the sink rate. With a further increase in the time period, the wake size below the intruder decreases, resulting in the resistance to the downward motion of the intruder. In summary, the wake dynamics above and below the intruder are responsible for the sink rate's non-monotonic behavior. At time periods $T \geq 2$, the square intruder experiences mostly a positive rate of vertical displacement. The square-shaped intruder shows a non-monotonic rise rate as a function of time period at $T \geq 2$, similar to that of the disk-shaped intruder. However, the square-shaped intruder has lower rise rates than that of the disk-shaped intruder. This is because the curved base of the disk-shaped intruder enables it to ascend the slant bed of particles more quickly than that of square one.

Figure 5 c displays the rise/sink rate of a rectangle-shaped (OS3) intruder as a function of time period. The rectangle-shaped intruder has a smaller base and a larger height. The rectangle-shaped intruder shows qualitatively similar behavior to that of the square-shaped one. However, at $T \leq 2$, the sink rate is smaller for the rectangle-shaped intruder (OS3) as compared to that of the square-shaped intruder(OS2). This is due to a smaller top surface of the rectangle-shaped intruder (4.5d) than that of the square-shaped one (6.5d), which yields in smaller stress experienced by the top surface of OS3 than that of OS2. Due to a small base, OS3 can climb the slant bed of particles more easily than that of OS2. This results in slightly higher rise rates for the OS3 shape than the OS2

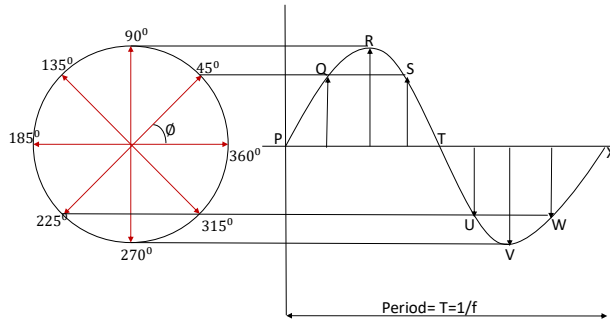


Figure 7: Oscillatory motion of the intruder as sine wave function representing the phase angle(φ)

one. For the rectangle-shaped intruder with a larger base and a smaller height (OS4), an opposite behavior is witnessed (figure 5 d). In this sense, the rise rate is smaller for OS4 as compared to that of OS3 and OS2. Moreover, the magnitude of the sink rate is greater for OS4 than that of OS2 and OS3 owing to the larger top surface of OS4. The rate of vertical displacement of the equilateral-triangle-shaped intruder (OS5) is shown in figure 5 e. The triangle-shaped intruder shows a mostly negative rate of vertical displacement because the V-shaped structure formed by its two edges at the vertices disables it to climb over the bed of particles. The intruder displayed a non-monotonic sink rate dependence on the time period. However, the magnitude of the sink rate is significantly higher than the other shapes considered in our study. The reason for it is due to an almost continual downward stress exerted by the particles on the triangle's slant edges. We have also found that there is an increase in the rate of rise of the intruder with the increase in the intergranular friction of $\mu = 0.0$ to 0.5 (figure 6). The same kind of trend has also been reported by Liu *et al.* (2021) for a 3D system with a circular intruder and also stated that there is a saturation of rise rate when $\mu \geq 0.5$.

Moreover, due to its unique geometry, each shape has a different angle of contact around its surface with the surrounding particles when oscillating horizontally. With square and rectangle shapes having a flat outer surface, triangular shape with an inclined angle, and disk with a smooth curvature. If we compare the positive V_y value which correspond to the rise of the intruder for the different shapes at $A/d = 3$ and 5 , than it is in the order of : $V_y; OS1 > V_y; OS3 > V_y; OS2 > V_y; OS4 > V_y; OS5$. Thus confirming that the geometric shape and orientation also affect the intruder's movement and its rate of rise in the system when oscillated horizontally.

3.3. Average rate of vertical displacement of an intruder with phase angle

In this subsection, we elucidate how the average rate of vertical displacement of the intruder varies with different positions of the oscillation cycle. One oscillation cycle involves the intruder travelling a distance of "A" from the centre to the right, then a distance of "2A" from right to the left, followed by a distance of "A" from left to the centre, where "A" is the amplitude. If we consider one oscillation cycle as a sine wave function, then each phase angle (φ) represents different horizontal positions of the intruder as shown in figure 7. Here, the phase angle $\varphi = 0$ or $10\varphi/\pi = 0$ represents

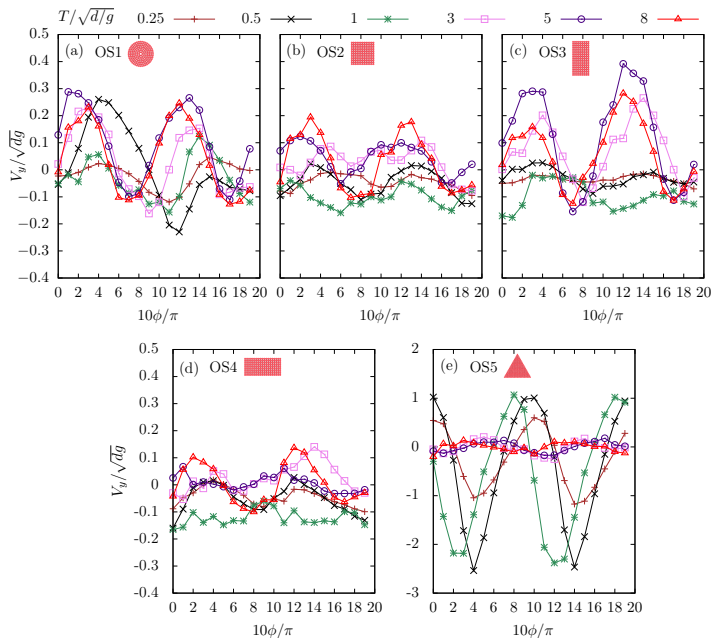


Figure 8: The rise rate(V_y) of the intruder vs the phase angle at $A/d = 3$ and different $T/\sqrt{d/g}$ for (a) disk, (b) square, (c) narrow-rectangle, (d) wide-rectangle, and (e) triangle shaped intruder object.

the centre point of oscillation when the intruder is moving from left to right, $\varphi = \pi/2$ or $10\varphi/\pi = 5$ indicates the rightmost point of oscillation. In the same way, $\varphi = \pi$ or $10\varphi/\pi = 10$ denotes the centre point of oscillation when the intruder is moving from right to left, $\varphi = 3\pi/2$ or $10\varphi/\pi = 15$ indicates the leftmost point of oscillation and $\varphi = 2\pi$ or $10\varphi/\pi = 20$ represents the centre point. Figure 8 a displays the average rate of vertical displacement (V_y) of the disk-shaped intruder as a function of its phase angle at different time periods and for an amplitude of $A/d = 3$. Here, V_y increases with φ from $10\varphi/\pi = 0$ to $10\varphi/\pi \approx 5$ where the intruder gradually climbs over the particles. When the intruder changes its direction of motion ($10\varphi/\pi = 5$) and moves from right to left, the wake to the left of the intruder gradually decreases. This is associated with an increase in the number of particles interacting with the intruder increasing the resistance to the vertical motion of the intruder. Therefore, V_y decreases from $10\varphi/\pi \approx 5$ to $10\varphi/\pi \approx 10$. However, from $10\varphi/\pi \approx 10$ to $10\varphi/\pi \approx 15$ the intruder again climbs over the particles yielding an increase in the average rate of vertical displacement V_y . When the intruder moves from left to right, another wake evolves to the right of it. At $10\varphi/\pi = 15$, the intruder changes its direction of motion and moves from right to left which results in a decrease in V_y due to the presence of wake to the right of the intruder. Interestingly, we witnessed both the positive and negative rates of vertical displacement in a single oscillation cycle at all timeperiods and for $A/d = 3$ for the disk-shaped intruder. At smaller timeperiods of oscillation, lower V_y is evidenced whereas, at larger timeperiods, greater V_y is noticed. This result is consistent with V_y as a function of time period (figure 5 a).

The square-shaped intruder (figure 8 b) shows qualitatively similar trends to that

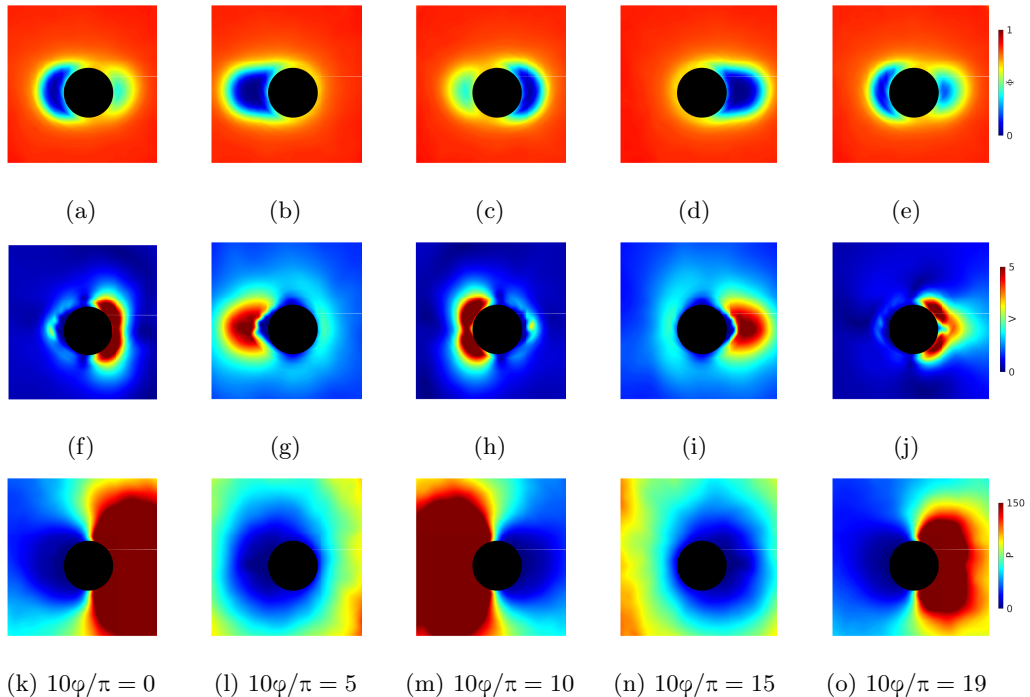


Figure 9: The time-averaged flow fields for depicting the area fraction Φ , velocity V and pressure P around the intruder OS1 (disk) for $T/\sqrt{d}/g = 1$ and different phase angle $10\varphi/\pi$: (a), (f), (k) 0.0, (b) (g), (l) 5.0, and (c), (h), (m) 10.0, (d), (i), (n) 15.0 and (e), (j), (o) 19.0. The oscillating amplitude of the intruder is $A/d = 3$.

of the disk-shaped one. The magnitude of V_y is greater for the disk-shaped intruder (OS1) as compared to that of a square-shaped one (OS2) although the diameter of OS1 (6.5d) and the side of OS2 (7.0d) are almost of the same length. The disk has a curved surface at the top whereas the square has a flat top surface and hence square-shaped intruder experiences greater stress from the particles above it than the disk-shaped one. This results in a smaller V_y for a square-shaped intruder as compared to that of a disk-shaped one. However, for a rectangle-shaped intruder having a shorter top surface (4.5d), a greater V_y is evidenced (figure 8 c) as compared to the square one, due to smaller stress experienced from the particles above it. For a rectangle-shaped intruder with a larger base (9.5d), we noticed a smaller V_y due to greater stress experienced by the intruder from the particles above it (figure 8 d). For a triangle-shaped intruder, we evidenced a negative rate of vertical displacement V_y for most of the phase angles. This could be due to its asymmetric geometry and either of the two inclining side walls experiencing stress from the particles above it throughout the oscillation cycle.

3.4. Mean flow fields

In this subsection, we have shown the time-averaged flow fields by using discrete microscopic data like velocities, positions, stress, etc., of each particle around the designated intruder region. The considered parameters such as the area fraction $\Phi(t)$, velocity $\mathbf{v}(t)$, stress tensor $\boldsymbol{\sigma}_{ij}(t)$ and the pressure $P(t)$ are calculated at any position \mathbf{p} with position vector \mathbf{r}_p and at an arbitrary time t as described in Glasser and Goldhirsch's

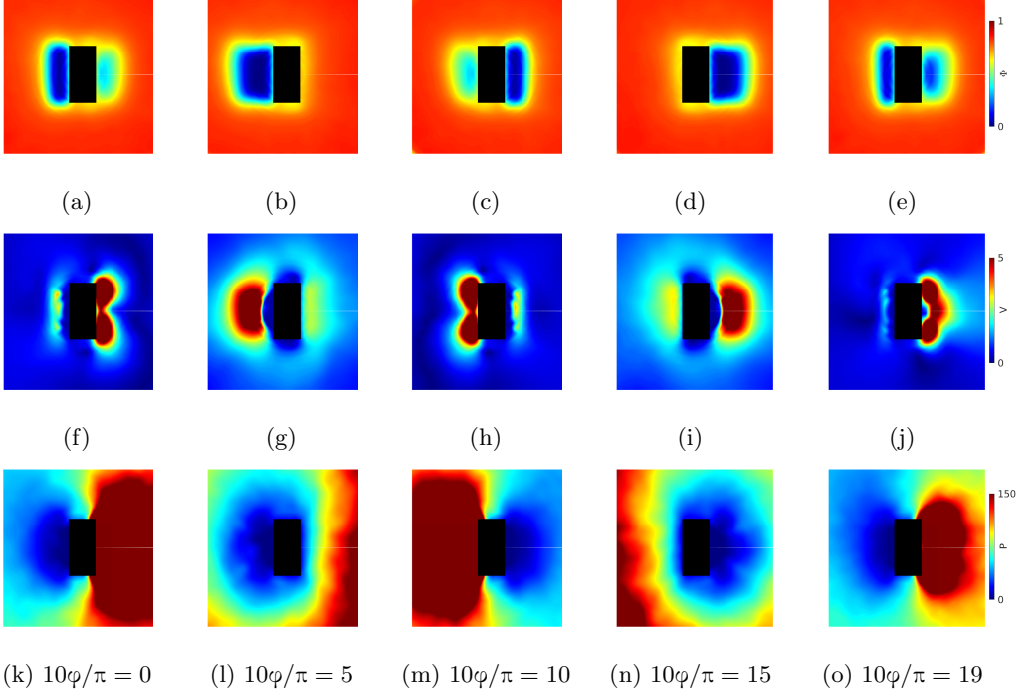


Figure 10: The time-averaged flow fields for depicting the area fraction Φ , velocity V and pressure P around the intruder OS3 (rectangle with its longer dimension along the y -axis) for $T/\sqrt{d/g} = 1$ and different phase angle $10\varphi/\pi$: (a), (f), (k) 0.0, (b) (g), (l) 5.0, and (c), (h), (m) 10.0, (d), (i), (n) 15.0 and (e), (j), (o) 19.0. The oscillating amplitude of the intruder is $A/d = 3$.

implementation of the Gaussian coarse-graining function (Glasser & Goldhirsch 2001; Dhiman *et al.* 2020; Reddy *et al.* 2021) :

$$\Phi(\mathbf{t}) = \sum_{i=1}^n \frac{\pi d_i^2}{4} \mathcal{W}(\mathbf{r}_p - \mathbf{r}_i(\mathbf{t})) \quad (3.1)$$

$$\mathbf{v}(\mathbf{t}) = \left[\sum_{i=1}^n \frac{\pi d_i^2}{4} \mathbf{v}_i \mathcal{W}(\mathbf{r}_p - \mathbf{r}_i(\mathbf{t})) \right] / \Phi \quad (3.2)$$

$$\boldsymbol{\sigma}_{ij}(\mathbf{t}) = \sum_{i=1}^n \sum_{j=i+1}^n (\mathbf{F}^{ij} \mathbf{r}_{ij}) \int_{s=0}^1 \mathcal{W}(\mathbf{r}_p - \mathbf{r}_i(\mathbf{t}) + s \mathbf{r}_{ij}) ds \quad (3.3)$$

$$P(\mathbf{t}) = \frac{-\text{tr}(\boldsymbol{\sigma}_{ij}(\mathbf{t}))}{2} \quad (3.4)$$

$$\mathcal{W}(\mathbf{r}) = \frac{1}{\pi w^2} e^{-r^2/w^2} \quad (3.5)$$

Here, $\mathcal{W}(\mathbf{r})$ is the coarse-graining function, ρ , d_i and $\mathbf{r}_i(\mathbf{t})$ are the density, diameter and the position vector of the particle i . \mathbf{F}^{ij} is the force on the particle i due to particle j and \mathbf{r}_{ij} is a vector in the direction of line joining the centres of two particles i and j . Moreover,

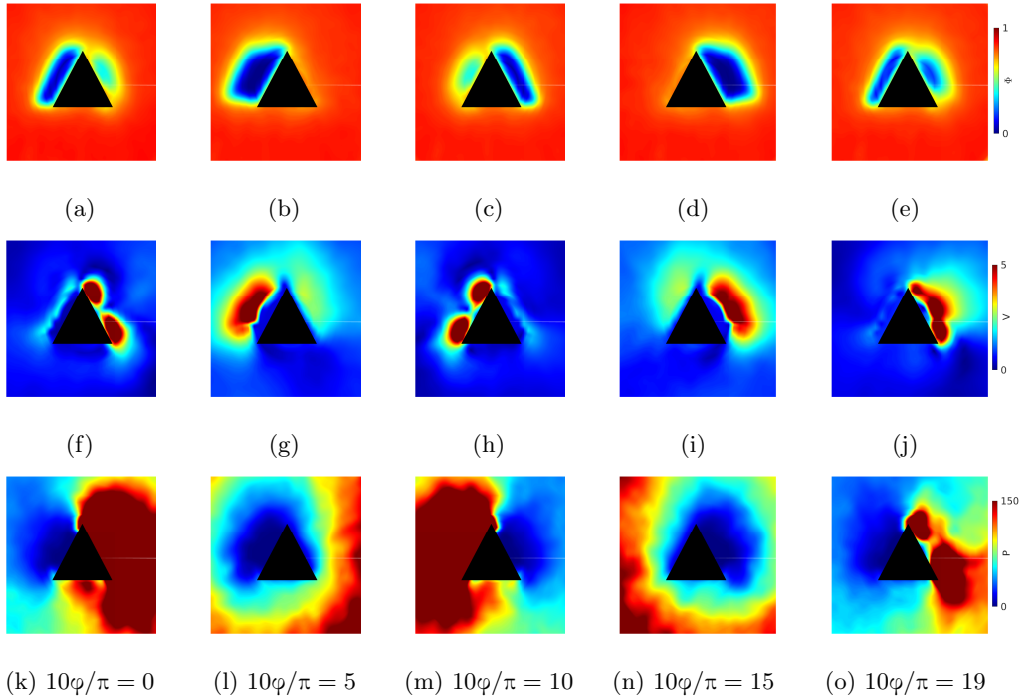


Figure 11: The time-averaged flow fields for depicting the area fraction Φ , velocity V and pressure P around the intruder OS5 (triangle) for $T/\sqrt{d}/g = 1$ and different phase angle $10\varphi/\pi$: (a), (f), (k) 0.0, (b) (g), (l) 5.0, and (c), (h), (m) 10.0, (d), (i), (n) 15.0 and (e), (j), (o) 19.0. The oscillating amplitude of the intruder is $A/d = 3$.

$w = 1.0$ and $\mathcal{W}(\mathbf{r}_p - \mathbf{r}_i) = 0$ if $|\mathbf{r}_p - \mathbf{r}_i| > 3w$ and φ, \mathbf{v} and P are the time-averaged area fraction, velocity and pressure. The flow fields presented are the region around the 15d radius from the centre of the intruder ($D_i = 5d$) and they are averaged over a minimum of 5000 frames.

Figure 9 displays the mean flow field of area fraction when the intruder is at the centre point of oscillation ($10\varphi/\pi = 0$) while it is moving from left to right. The area fraction is minimum in a small region on the left side of the intruder due to the development of wake. However, in a small region to the right side of the intruder, the area fraction is witnessed to be slightly lower than that of the bulk. In the above and below the regions of the intruder, the area fraction is almost the same as that of the bulk as the intruder can affect only those particles that are close to it. Figure 9 b shows the area fraction at the rightmost point of oscillation ($10\varphi/\pi = 5$) when the intruder has changed its direction of motion and has just started to move from right to left. A larger wake is witnessed to the left side of the intruder in this case as compared to that of the one in figure 9 a. However, this wake gradually disappears as the intruder moves from right to left as the particles surrounding the wake try to fill it due to the action of gravity. Consequently, by the time the intruder reaches the centre point of oscillation ($10\varphi/\pi = 10$), this wake is replaced by a mildly fluidized set of particles or in other words, a slightly smaller area fraction to the left of the intruder (figure 9 b). Moreover, another wake begins to develop to the right side of the intruder during this time. As the intruder reaches the rightmost point of oscillation ($10\varphi/\pi = 15$), a large trailing wake is evidenced to the right side of the intruder (figure 9 d). Moreover, the mildly fluidized bed to the left side of the intruder

is filled by particles above it and hence the area fraction becomes close to that of the bulk. Again as the intruder moves from right to left and reaches close ($10\varphi/\pi = 19$) to the centre point of oscillation, the wake to its right is slightly filled by particles and generating a fluidized bed (figure 9 e). A small region of dark blue to the left side of the intruder signifies the presence of another wake.

Figure 9 f illustrates velocity (V) fields when the intruder is at the centre point of oscillation ($10\varphi/\pi = 0$). The velocity is maximum on the right side of the intruder as the particles move along with the intruder while it is moving from left to right. The velocity is minimum in the regions above and below the intruder as the particles in this region are negligibly affected by the intruder's movement. The velocity of the particles on the left side of the intruder is significantly less than that on the right side. The reason for this might be due to a mildly fluidized bed of particles as noticed in figure 9 a. As the intruder moves from the centre point of oscillation ($10\varphi/\pi = 0$) to the rightmost ($10\varphi/\pi = 15$), a large wake is developed to the left side of the intruder as shown in figure 9 b. The particles surrounding the wake try to fill it with larger velocities which are represented by a region of red to the left of the intruder (figure 9 g). When the intruder moves from right to left, it pushes the particles to move along with it. This can be evidenced in figure 9 h: the zones of red colour to the left of the intruder. Figure 9 i shows the velocity field when the intruder is at the leftmost point of oscillation. The particle velocities on the left side of the intruder are slightly lower because the intruder has started to move towards the right. The regions of red colour at a certain distance from the right surface of the intruder represents the particles that are trying to fill the wake that is formed between them and the intruder. As the intruder moves from left to right, the intruder pushes the particles lying to its left and hence a region of red colour is seen in figure 9 j ($10\varphi/\pi = 19$).

Figure 9 k shows the pressure fields around the intruder when it is at the centre position of oscillation ($10\varphi/\pi = 0$). As the intruder is moving towards its right, greater pressure is noticed on the particles to the right. The zones of blue colour to the left of the intruder denotes the presence of wake. As the intruder starts to move towards its left after reaching the rightmost point ($10\varphi/\pi = 5$) of oscillation, the pressure on the particles to its right is small (figure 9 l). To the left of the intruder, pressure is very less due to the presence of wake as noticed in figure 9 b. When the intruder reaches the centre position ($10\varphi/\pi = 10$) from the right, the pressure is more to the left of the intruder (figure 9 m) as the intruder pushes the particles to its left while it is traversing. Figure 9 n shows the pressure when the intruder is at the leftmost point of oscillation. Very low pressure to the right of the intruder further confirms the presence of wake. Figure 9 o shows a greater pressure to the right of it as the intruder is moving towards its right.

Figure 10 shows the mean flow fields around a rectangle-shaped intruder with a small base length ($4.5d$) at different positions of oscillation. The wake region behind the rectangle-shaped intruder (figure 10 b and d) is larger than the disk-one (figure 9 b and d). The reason for this is the rectangle has a flat surface that pushes more particles while it is oscillating horizontally whereas, the disk with a curved surface can push fewer particles. Moreover, the y dimension length of the rectangle ($9.5d$) is larger than the diameter of the disk ($7.0d$). Due to the above-mentioned reasons, the regions of high velocities beside the wake are wider for the rectangle-shaped one (figures 10 g and i). The pressure fields are observed to be almost the same for both the disk-shaped and the rectangle-shaped intruders.

Figure 11 shows the mean flow fields of area fraction, velocity and pressure around an equilateral triangle-shaped intruder at different positions of oscillation. The pressure fields answer the question: why the triangle-shaped intruder has mostly a negative

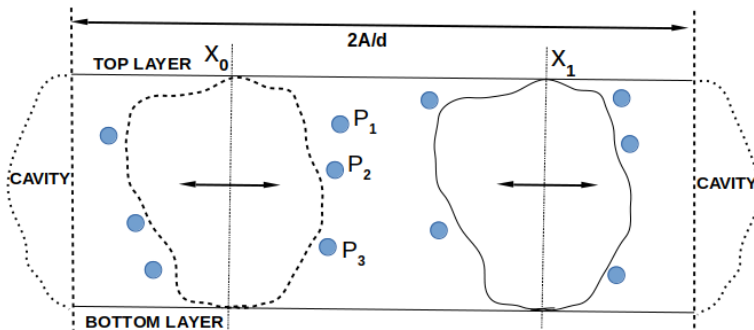


Figure 12: A general shape oscillating horizontally with granular particles around it.

vertical displacement. Either of the two slant faces of the intruder experience a vertical component of stress pointing downwards during its entire oscillation except when it changes its direction of motion. This can be witnessed in figures 11 k, 11 m and 11 o. In supplementary information we have also shown the mean flow fields around a square (Figure 1 in supplementary information) and a rectangle-shaped intruder (Figure 2 in supplementary information) with a large base length ($9.5d$) at different positions of oscillation.

3.5. Cavity model

We modeled the rising behaviour of the intruder by considering an arbitrary shape of the intruder and $(x, y) \in (\text{collection of points on the surface})$. In the granular medium, its position in the x direction is defined as $x_{\text{center of mass}} = A \sin(\omega t)$ (figure 12) owing to its horizontal oscillation. Now, if the orientation of an object is considered (with no rotational motion), then we can assign the axis such that $g = -|g|\hat{y}$ where $|g|$ is the magnitude of gravity. For the intruder to rise, an additional layer of particles has to form below the intruder as a result of free-fall in the cavity formed in the wake of the intruder. To form this additional bed, the particles surrounding the intruder have to drop below a certain point or threshold termed as “point of no return” and defined as a certain y -coordinate (y_{nr}), in a sense, if the particle’s y position is below y_{nr} , it becomes the part of the additional bed of particles. Therefore, the point of no return can be defined as a point on the surface of the intruder where tangent to its surface is $\pi/2$. In cases with multiple points on such surfaces, we assume that it is the lowest point on the surface because of its proximity to bottom layer. Consider an intruder placed at a position X_0 interacting with the particles P_1 , P_2 , and P_3 (figure 12). As the intruder moves from X_0 to X_1 position, it may be possible that particle P_3 will move down, whereas the particles P_1 and P_2 move upwards. So, we can say that the “point of no return” is somewhere in between the P_2 and P_3 position. This can be defined as the minimum y for which $\frac{dy}{dx} = \infty$.

Therefore, any granular particle around the intruder whose $y < y_{\text{nr}}$ will eventually settle to the bottom of the cavity. Let us also consider, the y -position of the top surface of the intruder as y_0 , then, a particle situated above the intruder has to move at least $(y_0 - y_{\text{nr}} + \frac{d}{2})$ in one-half time period ‘ T ’ of oscillation to be a part of the additional bed at the bottom. If one were to focus on the one-half oscillations such that at $t = 0$, it exists at one end of the cavity, and at $t = T/2$, it exists on the other end. When the intruder travels for time “ t ”, the net-free fall into the cavity begins at “ $-t$ ”. Therefore, the total time for net free-fall is “ $2t$ ” or a free-fall distance of $2gt^2$. The differential number

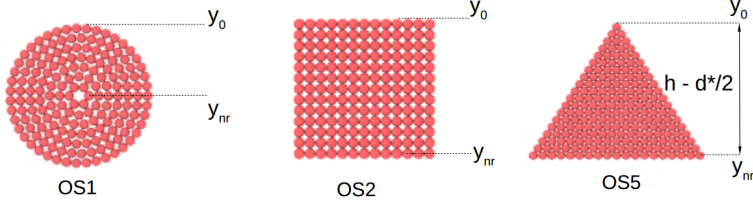


Figure 13: The shapes OS1, OS2 and OS5 with the points y_{nr} and y_0 where the particles covering this distance of $(l = y_0 - y_{nr})$ will fall beneath the base of the intruder.

of particles that cross the point of no return before the intruder approaches x at time t ,

$$dn = \frac{(2gt^2 - 1 - \frac{d}{2})4\varphi}{\pi d^2} dx; \quad (3.6)$$

$$dn = \frac{(2gt^2 - 1 - \frac{d}{2})4\varphi}{\pi d^2} \frac{2\pi A}{T} \sin\left(\frac{2\pi t}{T}\right) dt; \quad (3.7)$$

In equation 3.6, $l = y_0 - y_{nr}$ is the distance the particles have to cover to fall beneath the base of the intruder, and $(2gt^2 - 1 - d/2)$ is the height of the zone of the particles that have crossed the point of no return and reached the bottom of the intruder. The first particle crosses the point of no return at $\sqrt{(1 + \frac{d}{2})/2g}$, therefore, total particles reaching the bottom in one-half oscillation,

$$\int_0^N dn = \int_{\sqrt{\frac{1+\frac{d}{2}}{2g}}}^{T/2} \frac{(2gt^2 - 1 - \frac{d}{2})4\varphi}{\pi d^2} \frac{2\pi A}{T} \sin\left(\frac{2\pi t}{T}\right) dt; \quad (3.8)$$

$$N = \frac{4\varphi 2\pi A}{\pi d^2 T} \int_{\sqrt{\frac{1+\frac{d}{2}}{2g}}}^{T/2} (2gt^2 - 1 - \frac{d}{2}) \sin\left(\frac{2\pi t}{T}\right) dt; \quad (3.9)$$

Assuming $l' = 1 + \frac{d}{2}$ and Λ to be the integral part,

$$\Lambda = \frac{T^2}{4\pi} \left(\left(1 - \frac{2}{\pi^2}\right) gT - \frac{2l'}{T} - \frac{2}{\pi^2} gT \cos\left(\frac{2\pi}{T} \sqrt{\frac{l'}{2g}}\right) - \frac{4}{\pi} g \sqrt{\frac{l'}{2g}} \sin\left(\frac{2\pi}{T} \sqrt{\frac{l'}{2g}}\right) \right) \quad (3.10)$$

If we are to assume, the particles in the cavity form a uniform layer at the bottom of cavity, then, the rate of rise V_y can be given as elevation per half-oscillation and net oscillation as $N\pi(d^2/4)/(\varphi 2A)$,

$$V_y = \frac{4\varphi 2\pi A}{\pi d^2 T} \Lambda \frac{\pi d^2/4}{\varphi 2AT/2}; \quad (3.11)$$

$$V_y = \frac{2\pi}{T^2} \Lambda; \quad (3.12)$$

$$V_y = \frac{1}{2} \left(\left(1 - \frac{2}{\pi^2}\right) gT - \frac{2l'}{T} - \frac{2}{\pi^2} gT \cos\left(\frac{2\pi}{T} \sqrt{\frac{l'}{2g}}\right) - \frac{4}{\pi} g \sqrt{\frac{l'}{2g}} \sin\left(\frac{2\pi}{T} \sqrt{\frac{l'}{2g}}\right) \right) \quad (3.13)$$

Shape	l or (l' - d/2)	T _{rising} (cavitymodel)	T _{rising} (observed)
OS1	3.50	2.82	2.5-3.0
OS2	6.50	3.74	3.0-4.0
OS3	9.50	4.47	3.0-4.0
OS4	4.50	3.16	2.0-3.0
OS5	8.22	4.17	4.0-5.0

Table 1: Comparison between value of T_{rising} from theoretical estimate and the numerical simulations for an oscillating amplitude A/d = 5.

This equation describes V_y with respect to T for a given shape (fixed l'). For V_y = 0, we get

$$T_{\text{rise}} = \sqrt{2l'/g} \quad (3.14)$$

$$V_y = \frac{gT}{2} \left(\left(1 - \frac{2}{\pi^2}\right) - \left(\frac{T_{\text{rise}}}{T}\right)^2 - \frac{2}{\pi^2} \cos\left(\pi \frac{T_{\text{rise}}}{T}\right) - \frac{2}{\pi} \frac{T_{\text{rise}}}{T} \sin\left(\pi \frac{T_{\text{rise}}}{T}\right) \right) \quad (3.15)$$

Additionally, V_y cannot increase indefinitely with T due to cavity filling up. At some T_{max} ≈ √(8h/g), it will start to decrease with

$$V_y \approx \frac{h-1}{T} \quad (3.16)$$

showing an inverse relationship with timeperiod (T) at higher T as observed in all the cases. Here, "h" indicates the height of the oscillating object.

To summarise,

$$V_y = \begin{cases} \frac{gT}{2} \left(\left(1 - \frac{2}{\pi^2}\right) - \left(\frac{T_{\text{rise}}}{T}\right)^2 - \frac{2}{\pi^2} \cos\left(\pi \frac{T_{\text{rise}}}{T}\right) - \frac{2}{\pi} \frac{T_{\text{rise}}}{T} \sin\left(\pi \frac{T_{\text{rise}}}{T}\right) \right), & \text{if } T_{\text{rise}} < T < T_{\text{max}} \\ \frac{h-1}{T}, & \text{if } T > T_{\text{max}} \end{cases} \quad (3.17)$$

From Eqn. 3.15, we can say that an intruder can not sink when it is oscillated above its critical time period. The model will hold as long as the length of cavity is greater than one particle diameter, i.e., 2A > d or A > d/2, declaring A_{min} ≈ d/2 for all the intruder which is consistent with our results. The sinking regime is induced by the fluidization of granular bed of the cavity and is more complicated to predict while taking into account the shape of the intruder. We have shown the vertical velocity by colormaping it as a function of A and T in figure 14 for all the intruder shapes.

4. Conclusions

In the present work, we analyzed the vertical dynamics of a horizontally oscillating intruder (various shapes considered) via a numerical simulation method. Depending on the oscillation amplitude and time-period, the intruder can rise, sink, or almost remain in its initial position.

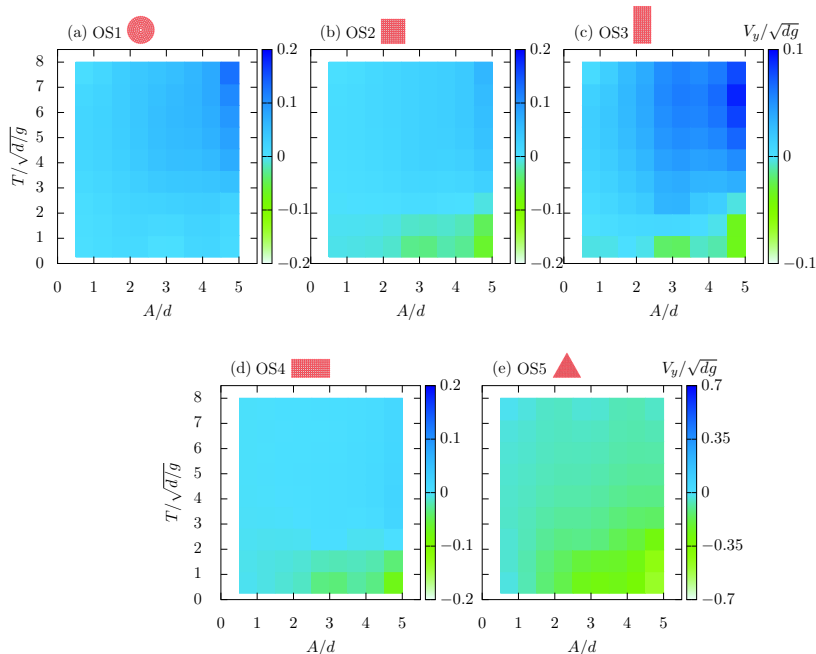


Figure 14: The colormap represents the rise rate V_y of the intruder (a) disk, (b) square, (c) narrow-rectangle, (d) wide-rectangle, and (e) triangle for all the oscillated T and A .

4.1. Vertical displacement of oscillating intruder

The vertical displacement of the intruder is sensitive to its oscillation parameters. We found that the intruder object rises in the granular medium at a high time period and sinks when oscillated at a low time period for $A/d > 1$. However, the triangular intruder is observed to have a negligible rise even when it is oscillated at a high time period. The final vertical settling position of the intruder changes non-monotonically with the time period of oscillation.

4.2. Rate of rise or sink of intruder with time-period

The shape of the intruder has a significant influence on its rate of climb or sink within the granular medium. We observed a maxima and minima for the rate of rise and sink for all the intruder shapes. The rate of sink was found to be the highest for $T / \sqrt{dg} = 1$ for all the intruder shapes when oscillated at $A/d = 3$ and 5 . Among all the shapes, we found that the disk (OS1) has the higher rate of rise, and triangle (OS5) has the higher rate of sink.

4.3. Average rate of vertical displacement of an intruder with phase angle

The average rate of vertical displacement of the intruder varies with phase angle (Figure 7). The phase angle $\varphi = 0$ or $10\varphi/\pi = 0$ represents the centre point of oscillation when the intruder is moving from left to right, $\varphi = \pi/2$ or $10\varphi/\pi = 5$ indicates the rightmost point of oscillation. The V_y increases with φ where the intruder gradually climbs over the particles. While there is a gradual decrease in V_y at certain range of phase angle which can

be attributed to greater number of particles in the path of oscillating intruder providing a greater resistance and hampering the intruder's positive vertical displacement.

4.4. Mean flow fields

The mean flow fields are reported for different phase angles around the intruder. The velocity field around the intruder shows that flow velocity is more on one side of the oscillating direction for the different phase angles. The pressure field around each intruder is asymmetric for different phase angles due to the wake formation. The area fraction field is observed to be less on one side and more on the other side due to the wake formation either to the left side of the intruder or to the right side, depending on its direction of motion. At the same time, the area fraction in the regions above and below the intruder is nearly equal to that of the bulk.

4.5. Cavity Model

We developed a theoretical model to predict motion of intruders oscillating in the granular medium at a specific amplitude and time period. The model was able to identify a critical time period, below which an oscillating intruder will not rise. For all the intruder shapes, a point of no return was proposed; if the granular particle passes this point, it will enter the cavity. These particles settling in the cavity will help the intruder to climb on them and rise.

4.6. Scope for future work

It will be interesting to study (i) the effect of the nature of the constituent granular particles on the rise/sink dynamics of oscillating intruders, (ii) the impact of orientation for a triangular intruder on its rise or sink (iii) effect of the aspect ratio of the cylinder intruder on its vertical dynamics, and (iv) the rise and sink dynamics of horizontally oscillating intruder in a three-dimensional granular medium.

Acknowledgement

We thank PARAM-ISHAN, the high-performance computing facility of IITG, where the simulations were performed.

Declaration of Interests: The authors report no conflict of interest.

REFERENCES

- BRILLIANTOV, NIKOLAI V, SPAHN, FRANK, HERTZSCH, JAN-MARTIN & PÖSCHEL, THORSTEN 1996 Model for collisions in granular gases. *Physical review E* **53** (5), 5382.
- CLARK, ABRAM H., KONDIC, LOU & BEHRINGER, ROBERT P. 2012 Particle scale dynamics in granular impact. *Phys. Rev. Lett.* **109**, 238302.
- CLARK, ABRAM H., PETERSEN, ALEC J. & BEHRINGER, ROBERT P. 2014 Collisional model for granular impact dynamics. *Phys. Rev. E* **89**, 012201.
- CUNDALL, PETER A & STRACK, OTTO DL 1979 A discrete numerical model for granular assemblies. *geotechnique* **29** (1), 47–65.
- DHIMAN, MANISH, KUMAR, SONU, REDDY, K ANKI & GUPTA, RAGHVENDRA 2020 Origin of the long-ranged attraction or repulsion between intruders in a confined granular medium. *Journal of Fluid Mechanics* **886**.
- DING, YANG, GRAVISH, NICK & GOLDMAN, DANIEL I 2011 Drag induced lift in granular media. *Physical review letters* **106** (2), 028001.
- GLASSER, BJ & GOLDBIRSCHE, I 2001 Scale dependence, correlations, and fluctuations of stresses in rapid granular flows. *Physics of Fluids* **13** (2), 407–420.

- GOLDMAN, DANIEL I. 2014 Colloquium: Biophysical principles of undulatory self-propulsion in granular media. *Rev. Mod. Phys.* **86**, 943–958.
- GOLDMAN, DANIEL I. & HU, DAVID L. 2010 Wiggling through the world: The mechanics of slithering locomotion depend on the surroundings. *American Scientist* **98** (4), 314–323.
- GUILLARD, FRANÇOIS, FORTERRE, YOËL & POULIQUEN, OLIVIER 2014 Lift forces in granular media. *Physics of Fluids* **26** (4), 043301.
- HU, DAVID L., NIRODY, JASMINE, SCOTT, TERRI & SHELLEY, MICHAEL J. 2009 The mechanics of slithering locomotion. *Proceedings of the National Academy of Sciences* **106** (25), 10081–10085, arXiv: <https://www.pnas.org/content/106/25/10081.full.pdf>.
- HUANG, LING, RAN, XIANWEN & BLUMENFELD, RAPHAEL 2016 Vertical dynamics of a horizontally oscillating active object in a two-dimensional granular medium. *Phys. Rev. E* **94**, 062906.
- KUMAR, SONU, REDDY, K ANKI, TAKADA, SATOSHI & HAYAKAWA, HISAO 2017 Scaling law of the drag force in dense granular media. *arXiv preprint arXiv:1712.09057*.
- LI, CHEN, ZHANG, TINGNAN & GOLDMAN, DANIEL I 2013 A terradynamics of legged locomotion on granular media. *science* **339** (6126), 1408–1412.
- LIU, PING, RAN, XIANWEN, CHENG, QI, TANG, WENHUI, ZHOU, JINGYUAN & BLUMENFELD, RAPHAEL 2021 Locomotion of self-excited vibrating and rotating objects in granular environments. *Applied Sciences* **11** (5), 2054.
- MALADEN, RYAN D, DING, YANG, LI, CHEN & GOLDMAN, DANIEL I 2009 Undulatory swimming in sand: subsurface locomotion of the sandfish lizard. *science* **325** (5938), 314–318.
- MALADEN, RYAN D, DING, YANG, UMBANHOWAR, PAUL B & GOLDMAN, DANIEL I 2011*a* Undulatory swimming in sand: experimental and simulation studies of a robotic sandfish. *The International Journal of Robotics Research* **30** (7), 793–805.
- MALADEN, RYAN D, UMBANHOWAR, PAUL B, DING, YANG, MASSE, ANDREW & GOLDMAN, DANIEL I 2011*b* Granular lift forces predict vertical motion of a sand-swimming robot. In *2011 IEEE International Conference on Robotics and Automation*, pp. 1398–1403. IEEE.
- MARVI, HAMIDREZA, GONG, CHAOHUI, GRAVISH, NICK, ASTLEY, HENRY, TRAVERS, MATTHEW, HATTON, ROSS L, MENDELSON III, JOSEPH R, CHOSET, HOWIE, HU, DAVID L & GOLDMAN, DANIEL I 2014 Sidewinding with minimal slip: Snake and robot ascent of sandy slopes. *Science* **346** (6206), 224–229.
- MAZOUCHOVA, NICOLE, GRAVISH, NICK, SAVU, ANDREI & GOLDMAN, DANIEL I 2010 Utilization of granular solidification during terrestrial locomotion of hatchling sea turtles. *Biology letters* **6** (3), 398–401.
- MEIRION-GRIFFITH, GARETH & SPENKO, MATTHEW 2010 An empirical study of the terramechanics of small unmanned ground vehicles. In *2010 IEEE Aerospace Conference*, pp. 1–6. IEEE.
- PING, LIU, RAN, XIANWEN & BLUMENFELD, RAPHAEL 2020 Sink-rise dynamics of horizontally oscillating active matter in granular media: Theory. *arXiv preprint arXiv:2006.04160*.
- PLIMPTON, STEVE 1995 Fast parallel algorithms for short-range molecular dynamics. *Journal of Computational Physics* **117** (1), 1 – 19.
- RAIBERT, MARC, BLANKESPOOR, KEVIN, NELSON, GABRIEL & PLAYTER, ROB 2008 Bigdog, the rough-terrain quadruped robot. *IFAC Proceedings Volumes* **41** (2), 10822–10825.
- REDDY, A VAMSI KRISHNA, KUMAR, SONU & REDDY, K ANKI 2021 Granular particle-shape heterogeneous mixtures discharging through a silo. *Journal of Fluid Mechanics* **912**.
- SHARPE, SARAH S, DING, YANG & GOLDMAN, DANIEL I 2013 Environmental interaction influences muscle activation strategy during sand-swimming in the sandfish lizard *scincus*. *Journal of Experimental Biology* **216** (2), 260–274.
- SHARPE, SARAH S, KUCKUK, ROBYN & GOLDMAN, DANIEL I 2015 Controlled preparation of wet granular media reveals limits to lizard burial ability. *Physical biology* **12** (4), 046009.
- SILBERT, LEONARDO E, ERTAŞ, DENİZ, GREST, GARY S, HALSEY, THOMAS C, LEVINE, DOV & PLIMPTON, STEVEN J 2001 Granular flow down an inclined plane: Bagnold scaling and rheology. *Physical Review E* **64** (5), 051302.
- STUKOWSKI, ALEXANDER 2010 Visualization and analysis of atomistic simulation data with OVITO—the Open Visualization Tool. *MODELLING AND SIMULATION IN MATERIALS SCIENCE AND ENGINEERING* **18** (1).
- TRIPURA, BITANG KWRUNG, KUMAR, SONU, REDDY, K. ANKI & TALBOT, JU-

- LIAN 2021 Role of shape on the forces on an intruder moving through a dense granular medium. *Particulate Science and Technology* **0** (0), 1–11, arXiv: <https://doi.org/10.1080/02726351.2021.1983905>.
- URQUHART, JAMES 2010 Lizard-inspired robot can ‘swim’ through sand. *New Scientist* **206** (2766), 23.
- ZHANG, TINGNAN, QIAN, FEIFEI, LI, CHEN, MASARATI, PIERANGELO, HOOVER, AARON M, BIRKMEYER, PAUL, PULLIN, ANDREW, FEARING, RONALD S & GOLDMAN, DANIEL I 2013 Ground fluidization promotes rapid running of a lightweight robot. *The International Journal of Robotics Research* **32** (7), 859–869.
- ZHU, LIANGLIANG, YANG, PENGFEI, LI, FENG, WANG, KAI, SHUI, LANGQUAN & CHEN, XI 2021 On the snake-like lateral undulatory locomotion in terrestrial, aquatic and sand environments. *Journal of the Mechanics and Physics of Solids* **157**, 104629.